Pulse buildup from noise and intrinsic polarization of plasma-based x-ray lasers

Chul Min Kim, Karol A. Janulewicz,* and Jongmin Lee†

Advanced Photonics Research Institute, Gwangju Institute of Science and Technology, Gwangju 500-712, Republic of Korea

(Received 14 April 2011; published 28 July 2011)

The paper presents a theoretical analysis of the pulse buildup from the spontaneous noise level and variations in the intrinsic polarization state of x-ray lasers, devices utilizing amplified spontaneous emission in a high-gain medium. Maxwell-Bloch equations with incorporated randomness of spontaneous emission, atomic level degeneracy, and time-dependent gain are used to describe the wave nature of the amplification process properly. The dynamics of pulse growth and polarization variation are analyzed for the entire amplification process starting from the initial state of random noise to the full saturation. It is shown that, within the used one-dimensional model, the output pulse can be polarized to a substantial degree. These results provide the basic understanding of x-ray lasers in a wave-optics perspective.

DOI: 10.1103/PhysRevA.84.013834 PACS number(s): 42.55.Vc, 42.55.Ah, 42.25.Kb, 42.25.Ja

I. INTRODUCTION

X-ray lasers (XRLs) based on laser-produced plasma have evolved dramatically during the last decade. With the grazing incidence pumping geometry [1], the pump energy was reduced to less than 1 J [2], and the output pulses were shortened to nearly bandwidth-limited ones of a typical duration of about 5 ps [3]. Injection of high harmonics into XRLs realized strong, fully coherent XRL output [4,5] with a prospect to get a linearly polarized beam [6]. This progress was accompanied by attempts to understand the underlying mechanisms of XRL dynamics using numerical simulation. Most of the simulations were performed using the Frantz-Nodvik model [7,8], that is, rate equations of radiation intensity and atomic level populations [9], which were extended in the kinetic part to take into account complicated atomic level structure and various atomic processes. The basic dynamics of amplification and spatiotemporal formation of gain in typical situations were understood well with such a treatment. However, the salient wave properties such as polarization and coherence could not be addressed at all since the rate equations ignore the phases of radiation and medium polarization.

Maxwell-Bloch (MB) equations offer more comprehensive formulation including the wave features as they describe radiation as a classical field and matter as a quantum system [10]. These equations have been used to describe XRL dynamics, after being modified to include the elements relevant to the lasing process: three-dimensional propagation and coherence [11], radiation polarization and atomic level degeneracy [12], statistical randomness of spontaneous emission (SE) [13], pumping and decay processes typically described by hydrodynamics simulation of laser-plasma interaction [13,14], and nonadiabatic dynamics of medium response [15]. In fact, no attempt was undertaken to implement all these aspects in one model. This is probably due to the complexity of such an attempt. However, getting a trade-off between the simplicity and completeness of the physical description is worth a try.

In the present paper, we investigate, by solving numerically the MB equations, the fundamental dynamics of pulse buildup and radiation polarization in XRLs including most of the effects mentioned earlier. The elements of the model describing resonant interaction were incorporated in full detail while those describing pulse propagation and gain formation were treated in a simplified fashion but without losing the wave-optics perspective and self-consistency of radiation-matter interaction. The detailed formulation of the theoretical model is given in Sec. II. In Sec. III, the main results obtained by using the model are discussed: amplification of pulse energy, dynamics of pulse buildup from the random noise of SE up to a fully saturated signal, and origin of radiation polarization of XRL pulses with an idea of experimental proof. A brief summary and conclusion are given in Sec. IV.

II. THEORETICAL MODEL

To describe the generation process of an XRL pulse in a reasonable way, without losing generality and any of the crucial elementary effects, the treatment of spatial dimensions and gain dynamics were simplified in some aspects: one-dimensional propagation with uniform distribution in the transverse plane was assumed, and spatiotemporally varying gain and atomic decay processes were approximated by an effective time-dependent gain and relevant constants, respectively. Radiation polarization, atomic level degeneracy, statistical randomness of SE, and nonadiabatic dynamics of the medium response were incorporated in detail since these determine the fundamental properties of the XRL output pulse.

The lasing transition $3d^9 4d(^1S_0) - 3d^9 4p(^1P_1)$ of nickel-like silver (Ag^{+19}) was selected for analysis due to the abundant experimental reports about the lasing action with this element [16–19]. Its transition wavelength is 13.9 nm, at which high-quality x-ray optical elements are commercially available. Figure 1(a) shows schematically the atomic energy levels and sketches physical processes relevant to lasing.

A. Major kinetic processes in the active medium

According to the selection rules of the electric dipole transitions, the resonant optical transition between the state b and the state a_{-1} (alternatively, the state b and the state a_1) involves only the left-handed (right-handed) circular polarization component of the radiation propagating along

*kaj@gist.ac.kr
†leejm@gist.ac.kr

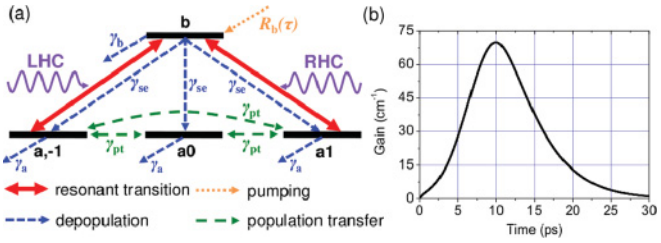

FIG. 1. (Color online) (a) Atomic energy level structure of and physical processes in an Ag^{+19} ion relevant to Ag^{+19}: $3d^9 4d(^1S_0)$ – $3d^9 4p(^1P_1)$ transition and (b) time-dependent gain of the medium. LHC (RHC) refers to the left-handed (right-handed) circular polarization component of radiation. The upper level $3d^9 4d(^1S_0)$ is denoted by the letter b and the lower one $3d^9 4p(^1P_1)$ by the letter a. The different states of the degenerate lower level are distinguished by their magnetic quantum numbers ($m = -1,0,1$). Various γ's refer to the rates of the relaxation processes.

the z axis [Fig. 1(a)] [12]. Population of the upper level [pumped at a rate of $R_b(\tau)$] and relaxation of this population are induced dominantly by inelastic electron-ion collisions while a minor contribution to the depopulation (at a rate of $3\gamma_{se}$) comes from SE. The total depopulation rate of the upper level is denoted by γ_b. In contrast, the depopulation of the lower level (at a rate of γ_a) occurs dominantly via fast radiative decay [20]. The population transfer among the different states of the degenerate lower level (at a rate of γ_{pt}) is due to elastic electron-ion collisions, which also contribute to dephasing of atomic dipoles (at a rate of γ_{dp}). Both level depopulation and atomic dipole dephasing determine the decay of medium polarization. The medium polarization decay rate γ_{ba} is given by $\gamma_{ba} = (\gamma_b + \gamma_a)/2 + \gamma_{dp}$ for homogeneous broadening [10]. This decay rate is related to the homogeneously broadened linewidth by the formula $\gamma_{ba} = \pi \Delta\nu_{FWHM}$ [21]. As a result of time-dependent pumping and depopulation, the medium demonstrates time-dependent gain [Fig. 1(b)] obtained from the hydrodynamics-atomic physics simulation with the EHYBRID code [22]. The peak small-signal-gain coefficient is equal to 70 cm^{-1}, and the temporal width [full width at half maximum (FWHM)] of the gain is estimated to be 10.9 ps.

B. Maxwell-Bloch equations

A real laser pulse is amplified in a spatiotemporally inhomogeneous medium with the parameters of relaxation and pumping varying both in space and in time. In such a case, a three-dimensional description is necessary to relate the computational results closely to the experimental values. As mentioned in the Introduction, we focused our attention on a simplified description to make essential physical processes to be also intuitively understood without losing the generality of the treatment. It was assumed that the medium is uniformly pumped in the ideal traveling-wave amplification scheme, and the pulse, uniform in the xy plane (plane wave front), propagates along the z axis. Hence, the spatiotemporal dependence of various relaxation parameters can be neglected, and variation of physical quantities is considered along only one spatial dimension and in time. With these approximations, the MB equations describing amplification process for the atomic level scheme presented in Fig. 1 are given as follows:

$$\partial N_b/\partial\tau = -\gamma_b N_b + \mathrm{Im}(P_R E_R^* + P_L E_L^*)/2 + R_b(\tau), \tag{1}$$

$$\partial N_{a,-1}/\partial\tau = -\gamma_a N_{a,-1} - \mathrm{Im}(P_L E_L^*)/2 + \gamma_{se} N_b + \gamma_{pt}(N_{a1} + N_{a0} - 2N_{a,-1}), \tag{2}$$

$$\partial N_{a1}/\partial\tau = -\gamma_a N_{a1} - \mathrm{Im}(P_R E_R^*)/2 + \gamma_{se} N_b + \gamma_{pt}(-2N_{a1} + N_{a0} + N_{a,-1}), \tag{3}$$

$$\partial N_{a0}/\partial\tau = -\gamma_a N_{a0} + \gamma_{se} N_b + \gamma_{pt}(N_{a1} - 2N_{a0} + N_{a,-1}), \tag{4}$$

$$\partial P_L/\partial\tau = -\gamma_{ba} P_L - i z_{ba}^2 [E_L(N_b - N_{a,-1}) + n_i \rho_{1,-1} E_R] + \Gamma_L(N_b,\tau), \tag{5}$$

$$\partial P_R/\partial\tau = -\gamma_{ba} P_R - i z_{ba}^2 [E_R(N_b - N_{a1}) + n_i \rho_{-1,1} E_L] + \Gamma_R(N_b,\tau), \tag{6}$$

$$\partial(n_i\rho_{1,-1})/\partial\tau = -\gamma_{1,-1} n_i \rho_{1,-1} + i(P_R^* E_L - P_L E_R^*)/4, \tag{7}$$

$$\partial E_L/\partial z = (i2\pi\omega_0/c)\left(P_L - n_e E_L/\omega_0^2\right), \tag{8}$$

$$\partial E_R/\partial z = (i2\pi\omega_0/c)\left(P_R - n_e E_R/\omega_0^2\right), \tag{9}$$

where N, P, and E refer to the population, complex amplitude of medium polarization, and complex amplitude of the electric field, respectively [23]. These variables are functions of propagation distance z and of the reduced time $\tau = t - z/c$. The subscripts L and R refer to left-handed circular (LHC) and right-handed circular (RHC) components of the beam polarization. The resonant frequency of the transition is denoted by ω_0, while n_e and n_i are electron and ion densities, respectively. The dipole matrix element of the resonant transition is denoted by z_{ba}. The complex random function Γ simulates the statistical character of SE [13]. The off-diagonal density matrix element $\rho_{1,-1}$ of the states a_1 and a_{-1} can be used as a measure of atomic coherence [10,24]. Its relaxation rate $\gamma_{1,-1}$ is given by the formula $\gamma_{1,-1} = \gamma_a + \gamma_{dp}$, in analogy with the formula for γ_{ba}.

The formulated equations were solved self-consistently [23]. Given an electric field at a fixed position, (1) through (7) are solved to obtain material response to radiation, and then the resulting medium polarization components are substituted into (8) and (9). These give the electric field at the next position. By repeating these steps, the spatiotemporal evolution of the interacting radiation and matter are described properly. The Runge-Kutta fourth-order algorithm was used for numerical solutions.

The complex random function Γ, emulating SE, is extremely spiky in time and cannot be properly expressed as a numerical sequence [13]. However, when integrated over short time interval (practically equal to the time step of the Runge-Kutta algorithm), it can be treated as a Gaussian random variable [25,26]. For the increment of medium polarization

P_L (P_R) over one time step, the contribution from Γ_L (Γ_R) is given simply as the value of the random variable [27]. The amplitude and phase of the medium polarization change randomly at every time step. A time step of 1 fs brought good convergence of the numerical solutions. Considering that more than 20 optical cycles of 13.9-nm radiation can reside within an interval of 1 fs, the randomness of SE is actually emulated by a sequence of wavelets of fixed duration and randomly varying complex amplitudes.

C. Determination of pumping function and physical parameters

The pumping function and the physical parameters were determined to match the medium parameter values known from the experiment and numerical simulation. The hydrodynamics-atomic physics code EHYBRID [22] was used to get $R_b(\tau)$, γ_b, γ_a, n_e, and n_i, the main parameters of the population kinetics. Atomic structure code MCDFGME [28] was used to get the SE rate γ_{se} and dipole matrix element z_{ba}. A typical value of linewidth $\Delta\lambda/\lambda = 5 \times 10^{-5}$ was used to calculate γ_{ba}. The dephasing rate γ_{dp} was calculated from γ_{ba}, γ_b, and γ_a.

The population transfer rate among the states of the degenerated lower level γ_{pt} was determined by noting that both dipole dephasing and atomic disalignment (a measure of the population imbalance between magnetic sublevels of a level [29]) are caused by the elastic electron-ion collisions. Given this, it seems reasonable to assume that the dephasing rate γ_{dp} is equal to the disalignment rate γ_{da}, that is, $\gamma_{dp} = \gamma_{da}$ [29–31]. As the degree of the disalignment is proportional to $(N_{a1} - 2N_{a0} + N_{a,-1})$ [29,32], its decay rate γ_{da} is connected to γ_{pt} by the relation $\gamma_{pt} = \gamma_{da}/3$ (consequently $\gamma_{pt} = \gamma_{dp}/3$), which can be derived from the kinetic equations describing the population transfer among N_{a_1}, N_{a_0}, and $N_{a_{-1}}$. Some authors used γ_{pt} calculated by applying the elastic electron-ion collision frequency of an equilibrium plasma [32]. In this case, γ_{pt} is much larger than γ_{dp}, which is inconsistent with the fact that both dephasing and atomic disalignment are caused by the elastic electron-ion collision.

The specific values of the parameters in the equations to be solved are as follows: $\hbar\omega_0 = 89.2$ eV, $\gamma_b = 2.6 \times 10^{12}$ Hz, $\gamma_a = 2.3 \times 10^{12}$ Hz, $n_e = 2.0 \times 10^{20}$ cm^{-3}, $n_i = 9.1 \times 10^{15}$ cm^{-3}, $\gamma_{se} = 5.9 \times 10^{10}$ Hz, $z_{ba} = 0.274$ a.u., $\gamma_{ba} = 3.4 \times 10^{12}$ Hz, $\gamma_{1,-1} = 3.3 \times 10^{12}$ Hz, and $\gamma_{pt} = 3.1 \times 10^{11}$ Hz. The beam cross section was assumed to be 400 μm^2, reasonably close to that of the experimentally observed beams.

III. RESULTS AND DISCUSSION

A. Amplification of pulse energy

The growth of the pulse energy with the propagation length exhibits the typical behavior of the amplified signal with a transition from the exponential increase to the linear one [16,18], as shown in Fig. 2. This rollover of the amplification curve is due to the onset of saturation, and the peak position of the second-order derivative of the curve can be used as the mark for the onset [33]. In Fig. 2, the saturation onset position is at $z = 3.1$ mm, at which the pulse energy is 33 nJ. A small-signal-gain coefficient of 55 cm^{-1}, reasonably consistent with the gain curve in Fig. 1(b) and the values

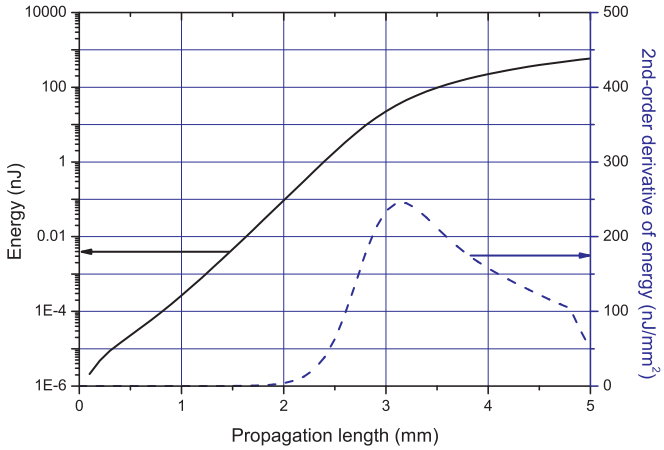

FIG. 2. (Color online) Pulse energy (solid line) its second-order derivative (dashed line) vs propagation length. The energy values were obtained by averaging the results from the 24 simulation runs with different random sequences.

reported in experiment, has been obtained by fitting the amplification curve between $z = 0.1$ mm and $z = 2$ mm to an exponential function. The pulse energy reaches 590 nJ at the end of the 5-mm-long medium.

B. Dynamics of pulse growth

The character of the pulse growth before saturation can be understood by taking notice of negligible affecting of the populations by the resonant interaction at this stage. In such a case, the terms involving E_L or E_R in (1) through (4) can be neglected, and, consequently, (1) through (4) can be solved independently of (5) through (9). Then the population inversions, $\Delta N_L = N_b - N_{a,-1}$ and $\Delta N_R = N_b - N_{a1}$, are given as functions of z and τ. Under the assumption of spatially uniform pumping, the dependence on z can be dropped [$R_b(z,\tau) = R_b(\tau)$], and ΔN_L and ΔN_R become the functions of τ only. As the influence of electric fields in (7) is negligible due to a low signal level, the density matrix element $\rho_{1,-1}$, initially equal to zero, also remains negligible. Then only (5), (6), (8), and (9) remain to be solved, and among them (5) and (8) describe only LHC components while (6) and (9) do only RHC. This separation implies that LHC and RHC signals grow independently of each other. The formal solution of either (5) and (8) or (6) and (9) is given by

$$E(z,\tau) = i\frac{2\pi\omega_0}{c}\int_0^z dz' \int_0^\tau d\tau' e^{-\gamma_{ba}(\tau-\tau')} \times \left[-iz_{ba}^2 E(z',\tau')\Delta N(\tau') + \Gamma(N_b(\tau'),\tau')\right], \quad (10)$$

where the subscripts L and R are suppressed. The form of the solution (10) let us conclude that the complex amplitude of output radiation is a weighted sum of the contributions from the net stimulated emission ($E\Delta N$) and SE (Γ) which have occurred at previous position (z') and at prior moment (τ'), with the weighting factor $e^{-\gamma_{ba}(\tau-\tau')}$.

At the beginning of the medium ($z = 0$ mm), SE acts as a random seed since the medium has no pre-existing radiation, and as a result the pulse shape is very spiky, as shown in Fig. 3(a). As the seed is amplified, the amplified signal

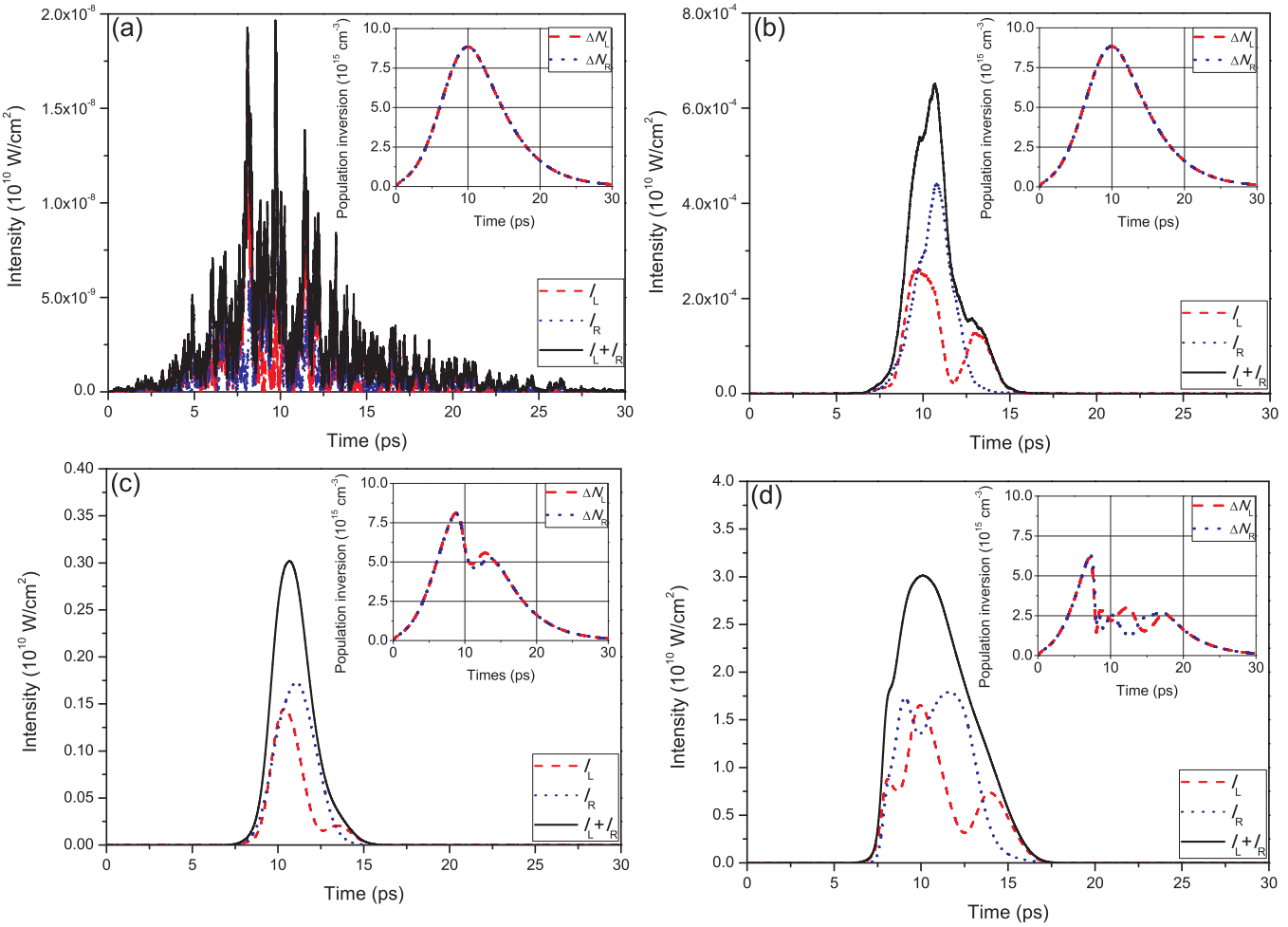

FIG. 3. (Color online) Temporal pulse profile at various positions in the amplifying medium: (a) $z = 0.1$ mm, (b) $z = 2$ mm, (c) $z = 3.1$ mm, and (d) $z = 5$ mm. The insets show the corresponding population inversions. I_L (I_R) refers to the intensity of the LHC (RHC), and ΔN_L (ΔN_R) refers to the population inversion relevant to the amplification of the LHC (RHC); that is, $\Delta N_L = N_b - N_{a,-1}$ ($\Delta N_R = N_b - N_{a1}$). Note that the intensity scale varies from figure to figure while the population scale remains the same.

surpasses quickly the level of the random SE seed and forms a well-defined pulse, as shown in Fig. 3(b). The shape of the pulse becomes smooth due to the spatiotemporal integration described by (10) as the pulse propagates through the medium. The LHC and the RHC intensities are independent of each other because they have started from the uncorrelated seeds. At this stage, the radiation is too weak to affect the medium properties, and the population inversion, or equivalently gain, shown in the insets of Figs. 3(a) and 3(b) differs hardly from the gain in Fig. 1(b). The amplification is exponential with propagation length, and the peak intensity grows from 2.0×10^2W/cm^2 at $z = 0.1$ mm to 6.5×10^6W/cm^2 at $z = 2$ mm.

As the radiation becomes strong enough to initiate saturation, it starts to affect the level populations, and consequently the gain of the medium becomes significantly modified as shown in the inset of Fig. 3(c). The pulse shape is very smooth, and both LHC and RHC wave components form single-peak pulses with the maxima around the time $\tau = 10$ ps because the gain is the strongest in the vicinity of this time point. Although the pulse components have started from the uncorrelated seeds, the time-dependent gain and smoothening effect have brought a shape similarity between them. The peak intensity at the saturation onset point is 3.0×10^9W/cm^2.

In a strongly saturated regime, the radiation noticeably influences the medium state, and this gives a feedback to the radiation. As a result, the Rabi oscillations of the population inversions and the corresponding oscillations of the radiation intensities are observed, as seen in Fig. 3(d). For each transition connected with a specific polarization component of radiation, the oscillations of population inversion and radiation intensity are anticorrelated; that is, the maximum of one corresponds to the minimum of the other. Moreover, the oscillations of both contributing intensities are anticorrelated as well. In both cases, anticorrelation occurs in space and time. This effect is a signature of the repeated energy exchange between radiation and medium. One can speak about the competition between two polarization components (modes) sharing a common upper laser level. To be more specific, let us consider the situation where LHC intensity is stronger than that of RHC at a given moment, but the population inversions, ΔN_L and ΔN_R, are almost equal. In such a case, ΔN_L, related to the stronger radiation component, decreases and begins to oscillate at the Rabi frequency corresponding

to the instantaneous level of LHC intensity. Reduction in gain of LHC is followed by reduction in the LHC intensity due to absorption accompanying Rabi oscillations in saturation. At the same time the weaker RHC sees stronger gain. This promotes RHC intensity to the stronger component and the procedure starts to be repeated but this time with ΔN_R. The population inversions on both transitions start to oscillate out of phase. As a result, the LHC and RHC intensities also start to oscillate out of phase. At $z = 5$ mm, the peak intensity is 3.0×10^{10}W/cm^2, and the pulse width (FWHM) is 5.2 ps, close to a measured average value of 5 ps [3].

The question arises as to how the length of our pulse is related to the reference given by a transform-limited pulse. Having transformed the radiation spectrum, we obtained the transform-limited pulse width of 1.3 ps (FWHM). Interestingly, if root-mean-square (rms) values were used to characterize the lengths of the modeled and bandwidth-limited pulses we obtained 2 and 1.7 ps, respectively. This differs significantly from 5.2 ps, the FWHM value of the modeled pulse. The deviation originates in the specific pulse shape. We are quoting both values as a rms value is always consistent with the uncertainty principle and constitutes the lower-bound value independent of a specific pulse shape. FWHM is more intuitive and practice-oriented value. The detailed analysis is beyond the scope of this paper.

As saturation strongly modifies and determines the final bandwith of the amplified radiation, we modeled the bandwith or gain narrowing in the amplification process as a function of the amplifier length. The plot is shown in Fig. 4. The most striking feature is clearly visible slower bandwidth decreasing in the very initial phase of the amplification. This is, we believe, caused by a very weak and random spontaneous signal. Such a behavior could contribute to explanation of the major discrepancy between measured and modeled linewidths in an XRL reported by Koch [34]. He obtained a significant misfit over the first 18% of the length while the theory and the experiment agreed perfectly within the medium remainder. For the given parameter set and using the formula

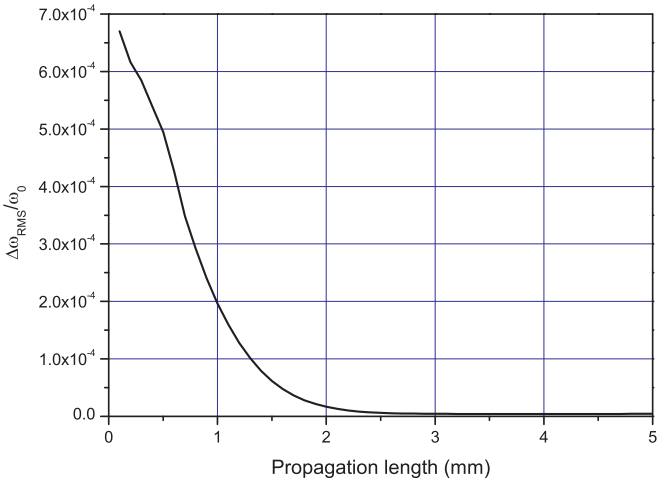

FIG. 4. (Color online) Gain narrowing during the amplification process shown as reduction in the bandwidth of the emitted radiation vs the medium length. Note the lower reduction rate for the first 0.5 mm of the medium length.

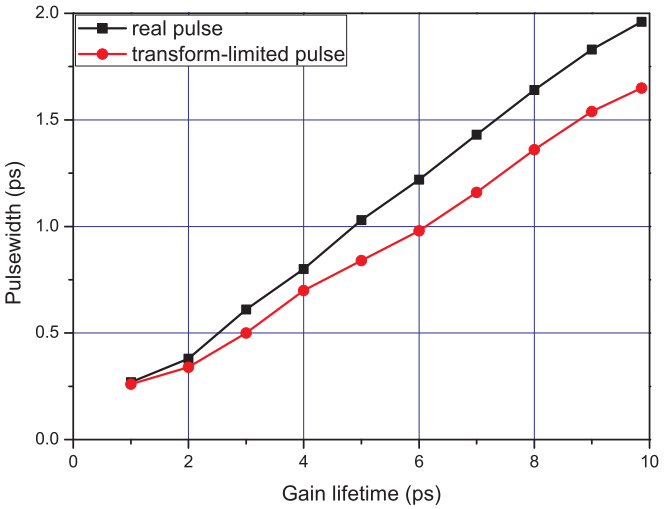

FIG. 5. (Color online) Pulse width (rms value) of the output pulse as a function of the gain lifetime (FWHM value) for two cases: modeled output pulse (upper trace) and the transform-limited pulse (lower trace). The medium length was assumed to be equal to 5 mm.

$\Delta\omega_a = \Delta\omega_0\sqrt{3/(G_{[dB]} - 3)}$ [35] we should expect narrowing by about one order of magnitude as it was confirmed by modeling.

To extend the applicable parameter set we modeled the output pulse shape for different lifetimes of the gain, keeping its peak value constant. It is expected for this type of laser that the pulse length is dominantly determined by the gain lifetime and is roughly proportional to this parameter (Fig. 5). This results from the fact that the gain lifetime determines the area of the gain medium from which radiation is effectively amplified. The plot in Fig. 5, drawn for rms values, indicates that also the bandwidth is strongly influenced by the gain dynamics and the transform-limited pulse length increases with the gain lengthening.

C. Polarization of radiation

As XRL pulses have their origin in SE that has a random polarization, no significant degree of polarization is commonly anticipated for XRL pulses. However, the modeling of the amplification process conducted here implies that substantial degree of polarization can be observed. Figure 4 shows variation of the degree of polarization (DOP) with the amplification length. DOP is essentially the normalized correlation between LHC and RHC [36]. For the propagation distance lower than 2.8 mm, which is close to the saturation onset point at $z = 3.1$ mm, DOP rises up to a high value of 0.85. Then it falls monotonically down to a value of 0.66 at $z = 5$ mm.

The increase of DOP before $z = 2$ mm is a result of time-dependent gain and spatiotemporal integration. As it was shown earlier, the intensities of both LHC and RHC grow mostly in the temporal region around $\tau = 10$ ps, where the gain is high, and their phase variations become moderate as the pulses are amplified. Two such spatiotemporally overlapped signals with moderate phase variation will have a high value of correlation. It should be stressed that this correlation between LHC and RHC appears not due to the atomic coherence

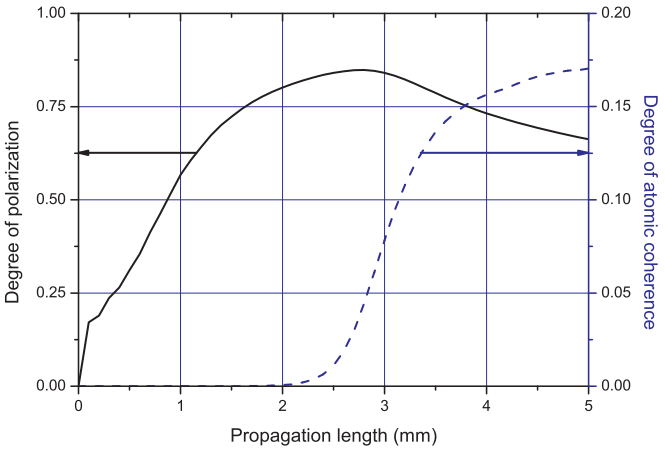

FIG. 6. (Color online) Degree of polarization (solid line) and degree of atomic coherence (dashed line) vs propagation length. We define degree of atomic coherence as the maximum value of $\rho_{1,-1}(z,\tau)|$ at a fixed position. The plotted values were obtained by averaging the results from the 24 simulation runs with different random sequences.

between a_{-1} and a_1 of the emitting medium but due to a general character of amplification in the weak-field limit. The atomic coherence, determining correlation between the quantum states of interest, is induced by strong-field coherent resonant interaction [10,23] and can be quantified by the maximum value of $|\rho_{1,-1}(z,\tau)|$, which we termed the degree of atomic coherence (DAC) between the states. When the electric fields are weak, the medium polarization components are proportional to the first order of the electric fields as implied by (5) and (6). Then, the cross-coupling term in (7) $(P_{\mathrm{R}}^{*}E_{\mathrm{L}} - P_{\mathrm{L}}E_{\mathrm{R}}^{*})$, which determines DAC, is proportional to the second order of the electric fields and thus negligible. Consequently, DAC keeps its initial value of zero. In Fig. 4, DAC remains close to zero up to the position of $z = 2$ mm, showing that the atomic coherence is negligible in the region.

Saturation of DOP is achieved between $z = 2$ mm and $z = 3$ mm, and after that DOP decreases monotonically. This effect is counterintuitive because DAC increases exactly in this region. The described situation suggests that the presence of two coupled strong optical transitions increases correlation between the states of the emitting medium and decreases correlation between the states of the emitted radiation. This situation is a consequence of anticorrelated oscillations of LHC and RHC in the saturation regime. Generally, the complex amplitudes (or phasors) E_{L} and E_{R} oscillate out of phase (are anticorrelated). As a result, the ratio of both components changes continuously with time and the condition $E_{\mathrm{L}}/E_{\mathrm{R}} = \text{constant}$, necessary to get DOP $= 1$ (well-defined polarization) [36], cannot be satisfied over the pulse duration. As the radiation becomes more intense in further propagation, more frequent variations of both components are developed within the pulse duration, which leads to further decrease in DOP.

The results presented above are obtained with a one-dimensional propagation model, and, strictly speaking, they describe the behavior of only a threadlike ray. The real three-dimensional beam can be approximated as a bunch of rays limited by the boundary conditions of the plasma column. In the beginning, these rays are not correlated because they are initiated by SE that has no spatial correlation. However, they diverge in the transverse direction and are coupled by overlapping; the transverse component of Laplacian, $\partial^2/\partial x^2 + \partial^2/\partial y^2$, of the wave equation is the coupling term. As a result, a beam of finite but relatively small cross-section can behave as a single ray. According to the results given above, such a narrow XRL beam can be distinctly polarized. The diameter of the part with well-defined polarization should be comparable to the spatial coherence length of the source because the coupling by divergence also induces spatial coherence. The specific polarization state would vary randomly from pulse to pulse, and further complication can be induced by the inhomogeneity of the medium, e.g., spatiotemporal dependence of the gain and refractive index.

The experimental observation of polarized XRL could be facilitated in the double-target setup [37], where the XRL pulse generated from the first target is injected as a seed into the second target. If the distance between the two targets is sufficiently long, the XRL pulse from the first target is spatially filtered by the limited cross-section of the second target and a beam consisting of the correlated rays can be obtained. Once the seed pulse is substantially polarized and sufficiently strong, the output pulse from the second target becomes polarized more strongly.

IV. CONCLUSION

We have analyzed the dynamics of XRLs in the wave-optics perspective by solving modified nonadiabatic MB equations. Three clearly distinguished phases of the process were identified: initiation from random SE, exponential amplification, and finally saturation. The underlying physics of the processes occurring in all these phases was explained in terms of the semicalssical model of radiation interaction with matter. Good agreement between the modeled output pulse shape and that recorded in experiment confirms correctness of the model. Furthermore, polarization of XRL radiation, a typical wave feature, was investigated, and the possibility of a reasonable DOP was numerically demonstrated along with a proposal for the experimental verification of the result. These results provide a fundamental understanding of x-ray lasing processes, which have become important as sources of strong coherent ultrashort x rays for various applications.

ACKNOWLEDGMENTS

This work was supported by the Ministry of Knowledge and Economy of Korea through the Ultrashort Quantum Beam Facility Program; by the Ministry of Education, Science and Technology of Korea through Basic Science Research Program (Grant No. R15-2008-006-03001-0) and Korea-Germany collaboration program (Grant No. 2010-00633); and by Gwangju Institute of Science and Technology through DASAN Project and Photonics 2020 project.

[1] R. Keenan, J. Dunn, P. K. Patel, D. F. Price, R. F. Smith, and V. N. Shlyaptsev, Phys. Rev. Lett. **94**, 103901 (2005).
[2] B. M. Luther, Y. Wang, M. A. Larotonda, D. Alessi, M. Berill, M. Marconi, J. J. Rocca, and V. N. Shlyaptsev, Opt. Lett. **30**, 165 (2005).
[3] M. A. Larotonda, Y. Wang, M. Berrill, B. M. Luther, J. J. Rocca, M. M. Shakya, S. Gilbertson, and Z. Chang, Opt. Lett. **31**, 3043 (2006).
[4] Ph. Zeitoun *et al*., Nature (London) **431**, 426 (2004).
[5] Y. Wang, E. Granados, F. Pedaci, D. Alessi, B. Luther, M. Berrill, and J. J. Rocca, Nat. Photon. **2**, 94 (2008).
[6] C. M. Kim, J. Lee, and K. A. Janulewicz, Phys. Rev. Lett. **104**, 053901 (2010).
[7] G. J. Pert, J. Opt. Soc. Am. B **11**, 1425 (1994).
[8] S. M. Hooker and D. J. Spence, J. Opt. Soc. Am. B **23**, 1057 (2006).
[9] L. M. Frantz and J. S. Nodvik, J. Appl. Phys. **34**, 2346 (1963).
[10] P. W. Milonni and J. H. Eberly, *Laser Physics* (Wiley & Sons, Hoboken, NJ, 2010).
[11] G. Hazak and A. Bar-Shalom, Phys. Rev. A **38**, 1300 (1988).
[12] A. Sureau and P. B. Holden, Phys. Rev. A **52**, 3110 (1995).
[13] O. Larroche, D. Ros, A. Klisnick, A. Sureau, C. Möller, and H. Guennou, Phys. Rev. A **62**, 043815 (2000).
[14] D. Benredjem, J. Dubau, O. Guilbaud, A. Klisnick, and C. Möller, Phys. High Energy Density **3**, 335 (2007).
[15] C. M. Kim, K. A. Janulewicz, H. T. Kim, and J. Lee, Phys. Rev. A **80**, 053811 (2009).
[16] G. J. Tallents, J. Phys. D: Appl. Phys. **36**, R259 (2003).
[17] P. Jaeglé, *Coherent Sources of XUV Radiation: Soft X-ray Lasers and High-Order Harmonic Generation* (Springer, New York, 2005).
[18] P. V. Nickles, K. A. Janulewicz, and W. Sandner, in *Strong Field Laser Physics*, edited by T. Brabec (Springer, New York, 2008), pp. 321–378.
[19] S. Suckewer and P. Jaeglè, Laser Phys. Lett. **6**, 411 (2009).
[20] G. J. Pert, Phys. Rev. A **50**, 4412 (1994).
[21] A. Yariv, *Quantum Electronics* (Wiley, New York, 1989).
[22] G. J. Pert, J. Fluid Mech. **131**, 401 (1983).
[23] B. W. Shore, *The Theory of Coherent Atomic Excitation* (Wiley, New York, 1990).
[24] R. W. Boyd, *Nonlinear Optics*, 2nd ed. (Academic Press, San Diego, 2003).
[25] S. Chandrasekhar, Rev. Mod. Phys. **21**, 383 (1949).
[26] J. C. Garrison, B. Ritchie, H. Nathel, C. K. Hong, and L. Minner, Phys. Rev. A **43**, 4941 (1991).
[27] C. Scherer, Braz. J. Phys. **34**, 442 (2004).
[28] MCDFGME (MultiConfiguration Dirac Fock and General Matrix Elements program, release 2005) edited by J. P. Desclaux and P. Indelicato [http://dirac.spectro.jussieu.fr/mcdf].
[29] T. Fujimoto, in *Plasma Polarization Spectroscopy*, edited by T. Fujimoto and A. Iwamae. (Springer, Berlin, 2008), pp. 91–126.
[30] A. Hirabayashi, Y. Nambu, M. Hasuo, and T. Fujimoto, Phys. Rev. A **37**, 83 (1988).
[31] H. R. Griem, *Principles of Plasma Spectroscopy* (Cambridge University Press, Cambridge, 1997).
[32] D. Benredjem, A. Sureau, B. Rus, and C. Möller, Phys. Rev. A **56**, 5152 (1997).
[33] C. Imesch, F. Staub, and J. E. Balmer, in *X-ray Lasers 2008*, edited by C. L. S. Lewis and D. Riley (Springer, Dordrecht, 2009), pp. 107–114.
[34] J. A. Koch, B. J. MacGowan, L. B. DaSilva, D. L. Matthews, J. H. Underwood, P. J. Batson, R. W. Lee, R. A. London, and S. Mrowka, Phys. Rev. A **50**, 1877 (1994).
[35] A. E. Siegman, *Lasers* (University Science Books, Mill Valley, CA, 1986), p. 281.
[36] M. Born and E. Wolf, *Principles of Optics* (Cambridge University Press, Cambridge, 2005).
[37] M. Nishikino, M. Tanaka, K. Nagashima, M. Kishimoto, M. Kado, T. Kawachi, K. Sukegawa, Y. Ochi, N. Hasegawa, and Y. Kato, Phys. Rev. A **68**, 061802(R) (2003).